Materials Transactions, Vol. 62, No. 8 (2021) pp. 1124 to 1132

Prediction of Work-Hardening Behavior under Various Loading Paths in 5083-O Aluminum Alloy Sheet Using Crystal Plasticity Models

Takayuki Hama[1,*1], Ryota Namakawa[1,*2], Yasuhiro Maeda[2] and Yasushi Maeda[2]

[1]*Graduate School of Energy Science, Kyoto University, Kyoto 606-8501, Japan*
[2]*Technical Development Group, KOBE STEEL, LTD., Kobe 651-2271, Japan*

In the present study, crystal plasticity models applicable for reproducing the work-hardening behavior under various loading paths of an A5083-O Al alloy sheet were examined. The loading paths under consideration were tension, reverse loading from compression to tension, simple shear, and biaxial tension. The accumulated-slip-based hardening model with the extended Voce hardening law provided good predictive accuracy for work-hardening behavior under uniaxial loadings. In contrast, it could not reproduce anisotropic hardening under biaxial tension, which was observed in the experimental results. In the case of dislocation-density-based hardening models, the work-hardening behavior under both uniaxial loadings and biaxial tension was reproduced fairly well when an anisotropic property in the interaction matrix was considered. On the basis of these results, a new accumulated-slip-based hardening model was proposed, in which the effects of latent hardening were considered in calculation of accumulated slip. The new model allowed prediction of anisotropic hardening under biaxial tension as in the case of the dislocation-density-based hardening model. This result suggested that the predictive accuracy of anisotropic hardening was more affected by the modelling of the latent hardening and interaction matrix than by the choice of internal variables of hardening, i.e., accumulated slip or dislocation density. [doi:10.2320/matertrans.MT-M2021020]

(Received February 2, 2021; Accepted May 19, 2021; Published July 2, 2021)

Keywords: *aluminum alloy sheet, crystal plasticity finite-element method, anisotropic hardening, reverse loading, simple shear, accumulated slip, dislocation density, latent hardening*

1. Introduction

Weight reduction in automobiles is a strongly desired outcome from the viewpoint of decreasing the environmental impact caused by vehicle use. In general, it is estimated that a reduction of 100 kg in automobile weight leads to a fuel-efficiency improvement of 1 km/l and a CO_2 gas emission reduction of approximately 9 g/km.[1,2] The substitution of lightweight materials for conventional steel sheets is considered one of the effective methods of realizing weight reduction. Among lightweight materials, Al alloys have come into wide use because of their low density and high recyclability. Nowadays, Al alloy sheets are used for automotive outer panels such as hoods, doors, front fenders, and roofs.[3]

In contrast to the abovementioned desirable properties of Al alloy sheets, there are still some challenges to its use due to some of its less-desirable material properties. For instance, a low Young's modulus (approximately one third that of steel) yields large springback,[4,5] and the pronounced plastic anisotropy of Al alloy sheets imposes difficulties in forming, which includes forming limit[6] and bendability.[7] Further, the elongation of Al alloy sheets is much smaller than that of mild steel sheets although the tensile strength and yield stress are comparable. This drawback also holds for 5000 series Al alloy sheets, which show comparatively large elongation in comparison to other types of Al alloy sheets. These characteristics hinder wider application of Al alloy sheets for automotive components. Hence, further investigation into the deformation behavior of Al alloy sheets, along with accurate prediction of formability using the finite-element method (FEM), are essential for extending the application of Al alloy sheets. To this end, work-hardening behaviors of Al alloy sheets under various loading paths and press formability have been studied both experimentally and numerically. Some recent works can be found in Refs. 6, 8–18).

Crystal plasticity models have also been widely used to model deformation behaviors in Al alloy sheets in recent years. Zhang *et al.*[19] investigated anisotropies in the yield stress and *r*-value of AA3103-H18 and AA3103-O sheets by conducting uniaxial tensile tests every 15° from the rolling direction (RD) to the transverse direction (TD). Five kinds of crystal plasticity models were also used to predict the in-plane anisotropies. These were the full-constraint Taylor model, Alamel model, Alamel type III model, viscoplastic self-consistent model, and crystal plasticity FEM. It was found that the Alamel-type models and crystal plasticity FEM yielded better predictive accuracy than the other models. Similar investigations were also conducted using an AA1050 Al sheet.[20] Brahme *et al.*[21] predicted stress–strain curves under plane-strain tension and equibiaxial tension of an AA5754 Al sheet using four different crystal-plasticity models for which material parameters were determined on the basis of a stress–strain curve under uniaxial tension. Work-hardening behavior was also evaluated beyond the onset of diffuse necking under uniaxial tension using crystal plasticity models. It was shown that the predicted work-hardening for large strains was dependent on the model, showing that the material parameters determined by curve fitting to experimental ultimate strength could not always accurately predict the material behavior under various loading paths. Hu *et al.*[22] used a full-constraint Taylor model, viscoplastic self-consistent model, and viscoplastic Fourier transform model to reproduce stress–strain curves and texture evolution under uniaxial tension, plane-strain tension, and equibiaxial tension of an AA5754 Al sheet. The

*[1]Corresponding author, E-mail: hama@energy.kyoto-u.ac.jp
*[2]Graduate Student, Kyoto University

results were also compared among the models. It was reported that the viscoplastic Fourier transform model provided the best prediction of texture evolution. In contrast, it was also found that the predictive accuracy of the mechanical responses was dependent on the loading path. Yoshida *et al.*[23] predicted the evolution of plastic contours of an AA3003-O sheet using two different crystal plasticity models, i.e., an accumulated-slip-based hardening model and a dislocation-density-based hardening model. Stress-path-dependent work-hardening was also shown to be qualitatively predicted using a dislocation-density-based model. Luo and Rousselier[24] proposed a new crystal plasticity model that could capture the strength-differential effect of an AA6260-T6 Al sheet. The proposed model could predict work-hardening behavior under various loading paths, including uniaxial tension, uniaxial compression, reverse loadings, biaxial tension, and pure shear. Zecevic and Knezevic[25] developed a polycrystal plasticity model based on an elasto-plastic self-consistent model and showed that the model could successfully simulate the Bauschinger effect and permanent softening under tension-compression cyclic loading tests on AA6022-T4 sheets. Hashimoto *et al.*[26] predicted the contours of plastic work of an AA5182-O sheet using a homogenized crystal plasticity FEM with a dislocation-density-based model and showed that an initial contour was predicted fairly well, whereas the following anisotropic hardening behavior was not reproduced by the model.

Several crystal plasticity models have been proposed with attendant predictive accuracies as discussed above. However, suitable models that can reproduce a variety of deformation behaviors that would occur during the sheet metal forming process are still open to discussion. Specifically, there are many studies on the predictive accuracy of uniaxial loadings, while only a few reports have been compiled on the predictive accuracy of the anisotropic hardening under biaxial tension, i.e., evolution of plastic contours.[23,26]

On the basis of the abovementioned background, the purpose of this study is that appropriate crystal plasticity models that can reproduce the work-hardening behavior of an AA5083-O Al alloy sheet will be examined under various loading paths including uniaxial tension, uniaxial reverse loading from compression to tension, simple shear, and biaxial tension. To this end, three different hardening models that were reported elsewhere will be used and the predictive accuracies of the deformation behaviors will be compared among them. Moreover, especially focusing on the prediction of anisotropic hardening, a new hardening model will be proposed.

2. Experimental Methods

2.1 Material

The material used in this study was a commercially-available Al alloy AA5083-O sheet with a thickness of 1.5 mm. Table 1 lists the mechanical properties of the sheet. Figure 1 shows the pole figures of the {001}, {110} and {111} planes obtained using electron backscatter diffraction (EBSD) measurements on an initial sample. The plane perpendicular to the rolling direction (RD) was measured,

Table 1 Mechanical properties of the material.

Tensile direction/°	E/GPa	σ_y/MPa	n	Lankford value
0	70.7	151	0.278	0.62
45	70.1	148	0.278	0.72
90	70.2	151	0.278	0.72

*E, σ_y, and n denote Young's modulus, yield stress, and work hardening exponent, respectively. Lankford values were measured at a nominal strain of approximately 0.1.

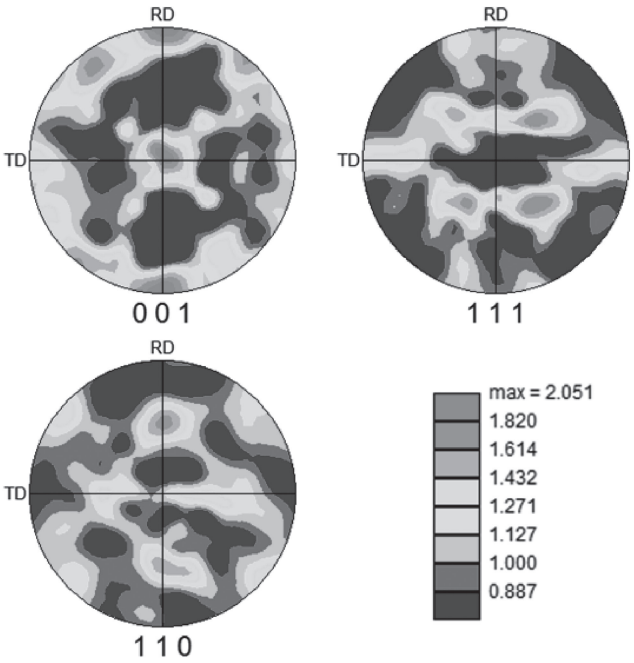

Fig. 1 Pole figures of A5083-O sheet.

and the results were analyzed using the software package OIM-Analysis (TSL Solutions). The step size was set to 2.0 μm in order to measure a relatively large area within a reasonable time-frame. The average grain size of the material was approximately 15 μm. The in-plane anisotropy of the properties was negligibly small, as shown in Table 1, presumably because of the weak texture. The results of the EBSD measurements were also used to determine initial crystallographic orientations used in crystal plasticity analyses.

2.2 Experimental procedures

2.2.1 Uniaxial tension and reverse loading

The uniaxial loading tests were conducted using a dumbbell-shaped sample with 10×20 mm in the gauge section. The digital image correlation (DIC) technique along with GOM Correlate Professional V8 (GOM) was used to evaluate strains.

Reverse loading tests from compression to tension with compressive strain of either 0.04 and 0.06 were conducted in the RD to examine the tension-compression asymmetry of the stress–strain curve as well as the Bauschinger effect. An experimental procedure of in-plane compression test was

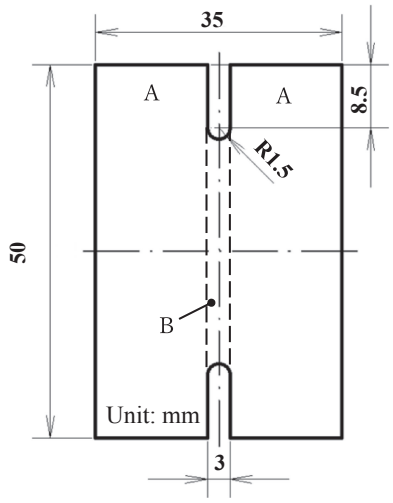

Fig. 2 Geometry of specimen for simple shear test.

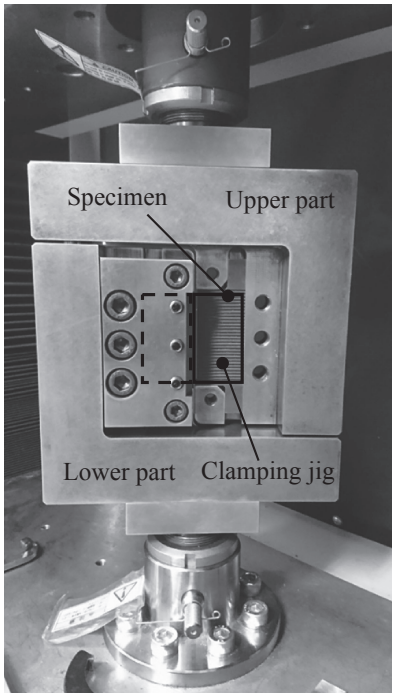

Fig. 3 Photograph of the testing device for simple shear test.

the same explained elsewhere.[27,28] A strain gauge (KFEM, Kyowa Electronic Instruments) was used to measure strains. The initial absolute strain rate was set to $1.0 \times 10^{-3}\,s^{-1}$.

Because the in-plane anisotropies of stress–strain curves and the Lankford values were small, only the results of the RD are shown in the following.

2.2.2 Simple shear

Figure 2 shows the sample geometry. The notch geometry was designed to give large strains without involving fracture near the edges.[29,30] Figure 3 shows the testing device used for the simple shear test.[31] The upper part of the device was moved upward to provide shear deformation to the area B of the specimen shown in Fig. 2, while constraining the deformation in the transverse direction by firmly clamping the areas A of the specimen. The constraint resulted in small normal stresses in the transverse direction.[29] The average shear stress τ_{ave} was calculated as $\tau_{ave} = F/Lt$, where F is the test force, t is the thickness, and L is the length of the gauge region.

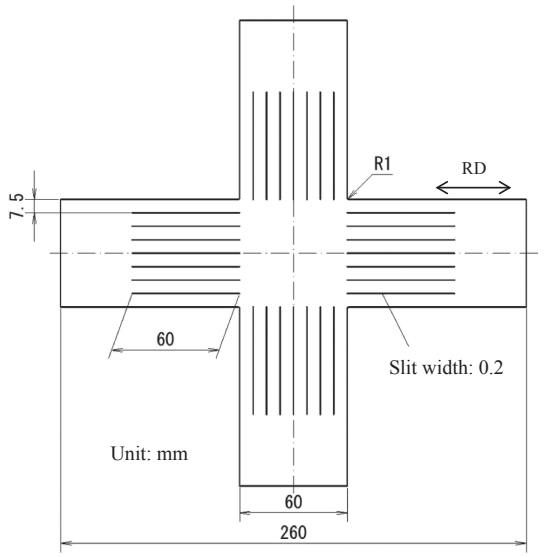

Fig. 4 Geometry of cruciform specimen for biaxial tensile test.[33]

It should be noted that the round notch of the specimen tended to yield nonuniform stress distributions near the edges; thus, the average shear stress τ_{ave} did not rigorously evaluate the shear stress. However, our preliminary studies showed that the stress measurement error for the round-notched specimen was comparable to that of a rectangular-notched specimen that yielded more uniform stress distribution.[29] Therefore, we concluded that the effect of the errors on the following discussion is negligible.

Shear strain was evaluated by using the Hencky strain,[32,33] with which engineering shear strain was measured using DIC. The tests were performed at the initial shear strain rate of $\dot{\gamma} = 1.8 \times 10^{-3}\,s^{-1}$.

2.2.3 Biaxial tension

Biaxial tensile tests were conducted following ISO 16842.[34] A biaxial tensile testing apparatus[35,36] and a cruciform specimen[35] shown in Fig. 4 were used. Following a literature,[36] two strain gauges attached 21 mm away from the specimen center in the maximum force direction were used to measure the strain components in the RD and TD. The stress components in the RD and TD, which are denoted as σ_{11} and σ_{22}, respectively, were then calculated using these strains. A linear biaxial stress path was applied to the specimen by controlling the true stresses σ_{11} and σ_{22} to be σ_{11}:σ_{22} = 4:1, 2:1, 4:3, 1:1, 3:4, 1:2, or 1:4. The results of σ_{11}:σ_{22} = 1:0 and 0:1 were obtained from monotonic tensile tests in the RD and the TD, respectively. The equivalent strain rate was set to $5.0 \times 10^{-4}\,s^{-1}$.

3. Crystal Plasticity Finite-Element Method

3.1 Constitutive model of single crystal

Basic formulations and simulation procedures for a crystal plasticity finite-element method used in this study follow those explained in prior literature;[37–39] thus, they are only briefly explained here.

The face-centered cubic structure was assumed. 12 {111} ⟨110⟩ slip systems were considered. The slip rate of the α th

slip system $\dot{\gamma}^\alpha$ is related to the resolved shear stress τ^α by using the visco-plastic power law:[40–42]

$$\dot{\gamma}^\alpha = \dot{\gamma}_0 \left| \frac{\tau^\alpha}{\tau_Y^\alpha} \right|^{\frac{1}{m}} \mathrm{sign}(\tau^\alpha), \quad \tau^\alpha = \boldsymbol{s}^\alpha \cdot \boldsymbol{\sigma} \cdot \boldsymbol{m}^\alpha, \tag{1}$$

where $\dot{\gamma}_0$ is the reference slip rate, τ_Y^α is the slip resistance of the αth slip system with $\tau_Y^\alpha = \tau_0$ initially, where τ_0 is the initial critical resolved shear stress (CRSS), and m is the strain rate sensitivity exponent. $\boldsymbol{s}^\alpha$ and $\boldsymbol{m}^\alpha$ are the unit vectors that respectively represent the slip direction and the normal of the slip plane of the α th slip system. The rate of slip resistance is given by:

$$\dot{\tau}_Y^\alpha = \sum_\beta h_{\alpha\beta} |\dot{\gamma}^\beta|, \tag{2}$$

where $h_{\alpha\beta}$ is the hardening moduli matrix. In this work, accumulated-slip-based hardening and dislocation-density-based hardening models were used to describe the hardening moduli matrix and will be described in the next section.

3.2 Hardening models

3.2.1 Accumulated-slip-based hardening model

The hardening moduli matrix $h_{\alpha\beta}$ proposed by Hutchinson[43] is given by

$$h_{\alpha\beta} = [q + (1-q)\delta_{\alpha\beta}] h(\bar{\gamma}), \tag{3}$$

where q is the ratio between the latent-hardening rate and the self-hardening rate, $\delta_{\alpha\beta}$ is the Kronecker delta, and $h(\bar{\gamma})$ is the hardening rate based on accumulated slip: $\bar{\gamma} = \sum_\alpha \int_0^t |\dot{\gamma}^\alpha|$. The latent-hardening parameter q was set to 1.4.[44,45]

For the rate of hardening h, the following extended Voce hardening law was used:

$$h(\bar{\gamma}) = \theta_1 + \left(\theta_0 - \theta_1 + \frac{\theta_0 \theta_1}{\tau_1} \bar{\gamma} \right) \exp\left(-\frac{\theta_0 \bar{\gamma}}{\tau_1} \right), \tag{4}$$

where τ_1, θ_0 and θ_1 are the material parameters. This and similar hardening laws have been used to represent the deformation behavior of Al alloys.[e.g., 46–48]

3.2.2 Dislocation-density-based hardening model

The following dislocation-density-based hardening model[49,50] was utilized:

$$h_{\alpha\beta} = \frac{\mu}{2} g_{\alpha\beta} \left(\sum_\kappa g_{\alpha\kappa} \rho^\kappa \right)^{-\frac{1}{2}} \left[\frac{1}{K} \left(\sum_\kappa g_{\alpha\kappa} \rho^\kappa \right)^{\frac{1}{2}} - 2 y_c \rho^\beta \right], \tag{5}$$

where μ is the shear modulus, y_c is the characteristic length that represents the annihilation process of dislocation dipoles, K is a material parameter, and $g_{\alpha\beta}$ is the interaction matrix. ρ^α is the total dislocation density of the α th slip system and its evolution is given by

$$\dot{\rho}^\alpha = \frac{1}{b} \left(\frac{1}{L^\alpha} - 2 y_c \rho^\alpha \right) |\dot{\gamma}^\alpha| \tag{6}$$

with b being the magnitude of the Burgers vector. L^α is expressed as $L^\alpha = K / \sqrt{\sum_\kappa g_{\alpha\kappa} \rho^\kappa}$.

$g_{\alpha\beta}$ is a 12×12 matrix which has only six independent components,[51] whose coefficients have recently been estimated using dislocation dynamics simulations.[52–55]

It should be noted that back stresses were not considered in this study. However, as will be explained in the following sections, the reverse loading behavior including the Bauschinger effect could be accurately predicted, verifying this approximation.

3.3 Finite-element model

The crystal plasticity models explained in the previous sections were incorporated into a static FEM in which explicit time integration was utilized.[37] The representative volume element was a cube for the simulations of uniaxial and biaxial loadings. On the other hand, because preliminary studies suggested that the number of elements in the longitudinal direction was important for simple shear simulations, a cuboid with the length ratio $l{:}h{:}t = 30{:}3{:}1$, which denote respectively the longitudinal length, height, and thickness, was used for simple shear. The dimension of the cuboid was determined on the basis of the sample geometry of simple shear (Fig. 2). 8-nodes solid elements were used for discretization. The number of finite elements were 1000 for both models. Displacement boundary conditions were utilized to give prescribed loading paths.[56] Initial crystallographic orientations were randomly chosen from the result of the EBSD measurement and assigned to the integration points. The same crystallographic orientation was assigned to the eight integration points in each element.

3.4 Material parameters

The following three models were used: the accumulated-slip-based hardening model with the extended Voce hardening law (eq. (4)) (A model) and the dislocation-density-based model (eq. (5)) with two different interaction matrix parameters (D-1 and D-2[55] models). The components of $g_{\alpha\beta}$, i.e., g_0, g_1, g_2, g_3, g_4, and g_5, which denote respectively self-hardening, collinear system, Hirth lock, coplanar system, glissile junction, and Lomer–Cottrell sessile lock, of the D-1 and D-2 models are shown in Table 2.

The elastic constants were set to $C_{11} = 107\,\mathrm{GPa}$, $C_{12} = 61\,\mathrm{GPa}$, and $C_{44} = 28\,\mathrm{GPa}$.[57] The reference slip rate and the strain rate sensitivity exponent were taken to be $\dot{\gamma}_0 = 0.001\,\mathrm{s}^{-1}$ and $m = 0.002$, respectively.[39] For the dislocation-density-based model, the magnitude of the Burgers vector was set to $b = 2.86 \times 10^{-10}\,\mathrm{m}$ and the initial dislocation density ρ_0^α was taken to be $1.0 \times 10^{10}\,\mathrm{m}^{-2}$ regardless of the slip system.[23]

The hardening parameters were determined by fitting a stress–strain curve under uniaxial tension in the RD for a uniform elongation range, i.e., to a strain of approximately 0.2. Moreover, τ_1 in eq. (4) was slightly adjusted to fit the curve during tension following compression. The sets of parameters for each model are listed in Table 2.

4. Experimental and Simulation Results

4.1 Uniaxial loading

Figure 5 shows the true stress-true strain curves in the RD. In the experiment, yield elongation was observed. The serrated flow occurred after yielding, and it became more pronounced as the plastic deformation proceeded. Because the hardening parameters of the crystal plasticity models were

Table 2 Hardening parameters for crystal plasticity models.

	τ_0 (MPa)	τ_1 (MPa)	θ_0 (MPa)	θ_1 (MPa)
A	52	60	365	12
E-1	54	60	3500	435
E-2	56	70	150	80

	τ_0 (MPa)	K	y_c (m)	g_0	g_1	g_2	g_3	g_4	g_5
D-1	51	2.18	1.05×10^{-8}	0.122	0.122	0.122	0.122	0.122	0.122
D-2	51	5.00	1.05×10^{-8}	0.122	0.810	0.205	0.122	0.320	0.122

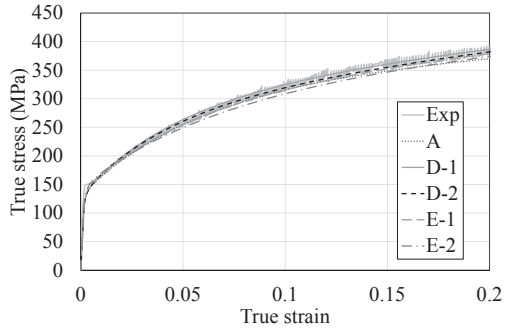

Fig. 5 True stress–true strain curves under uniaxial tension.

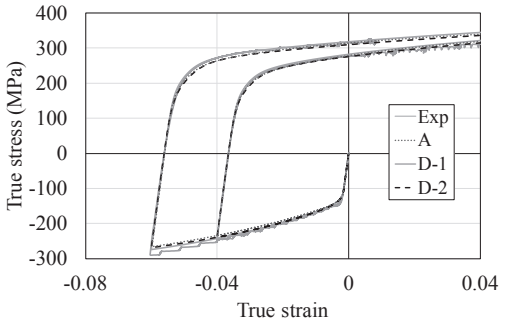

Fig. 7 True stress–true strain curves under reverse loading.

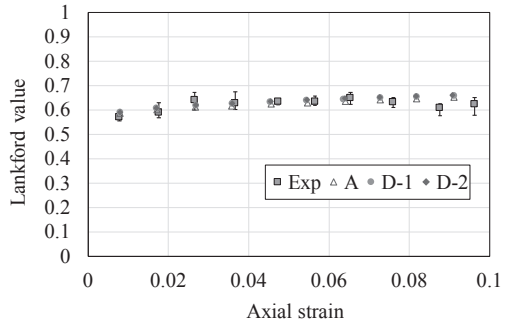

Fig. 6 Evolution of r-values under uniaxial tension.

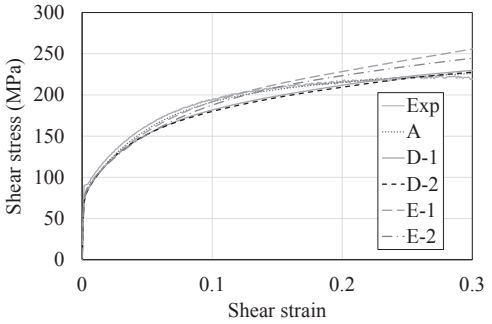

Fig. 8 Shear stress–shear strain curves under simple shear.

determined using this curve, the simulation results were almost within the serrated flow of the experimental curve in the whole range tested.

Figure 6 shows the evolution of the Lankford value measured for every 0.01 strain. The Lankford value was almost independent of the strain, and the simulation results agreed fairly consistently with the experimental results regardless of which model was used. Although detailed results are not provided, similar predictive accuracies were achieved in the TD and diagonal direction for stress–strain curves and Lankford values.

Figure 7 shows the true stress-true strain curves under reverse loading. The early re-yielding, i.e., the Bauschinger effect, was observed irrespective of the pre-strain. In the simulation results, the curve during compression, early re-yielding, and the flow stresses after stress reversal were in fairly good agreement with the experimental results regardless of the model.

4.2 Simple shear

Figure 8 shows the results of the shear stress-shear strain curves. The shear yield stress was approximately 90 MPa. The failure occurred from the circular edge of the shear region at a shear strain of approximately 0.28. The maximum shear stress was approximately 220 MPa. The yield elongation and serrated flow also appeared as in the tensile test (Fig. 5), but the serrated flow was much less pronounced than that of the tensile test.

The A model predicted the entire curve fairly well, especially the saturation of work-hardening for large strains. In contrast, the D-1 and D-2 models underestimated the stresses in the shear strain range from approximately 0.03 to 0.22, while they tended to overestimate the overall work-hardening.

4.3 Biaxial tension

Figure 9(a), 9(b), and 9(c) show the stress components of equal plastic work obtained for the A, D-1, and D-2

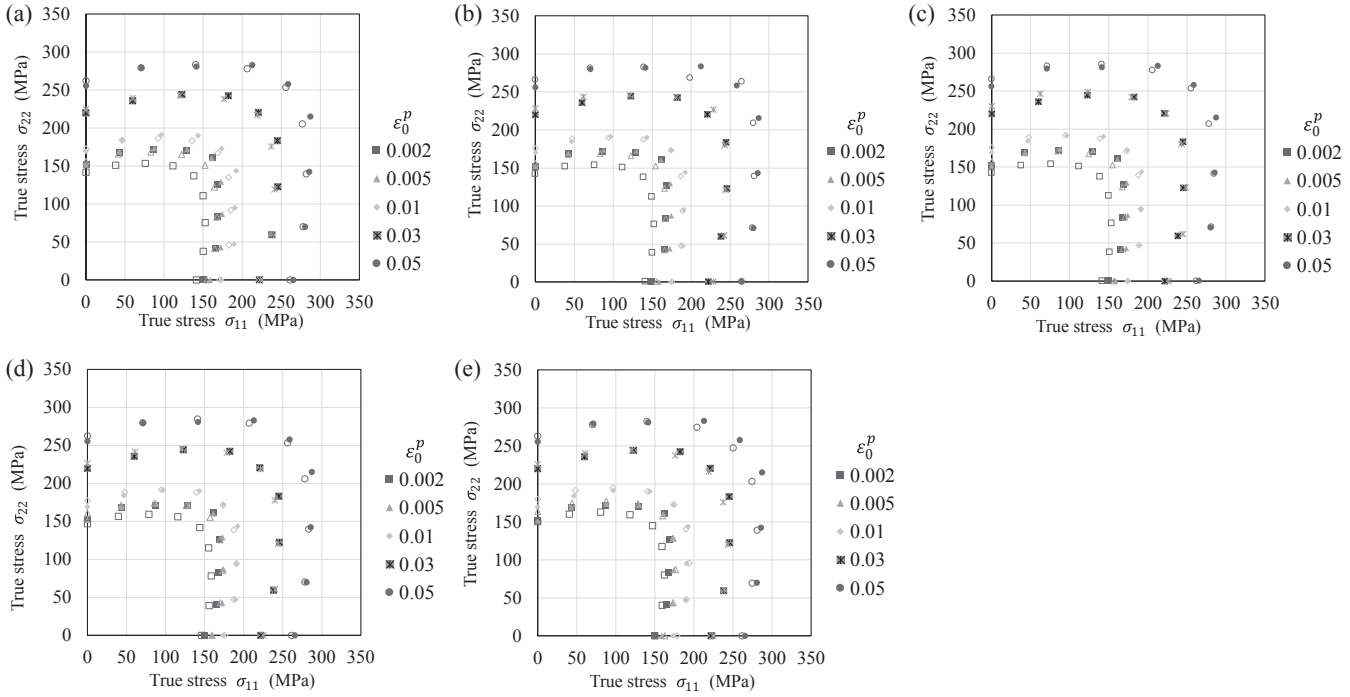

Fig. 9 Stress components of equal plastic work. σ_{11} and σ_{22} denote the stress components in the RD and TD, respectively. Solid and open circles represent experimental and simulation results, respectively. Simulation results are for the (a) A model, (b) D-1 model, and (c) D-2 model, (d) E-1 model, and (e) E-2 model.

models, respectively. The reference plastic strains, which correspond to strains under uniaxial tension, were set to $\varepsilon_0^p = 0.002$, 0.005, 0.01, 0.03 and 0.05. It should be noted that in the experimental results the averages of two samples are shown. The experimental error was at most 5 MPa under biaxial tension, and this difference was less than approximately 2% of the flow stress. In the experimental results, the stresses in the range of $\sigma_{11} > \sigma_{22}$ increased slightly from $\varepsilon_0^p = 0.002$ to 0.005, while those in the range of $\sigma_{11} \leq \sigma_{22}$ remained almost unchanged. This difference was owing to the difference in the amount of yield elongation. Thereafter, the stress points were nearly symmetrical with respect to the line $\sigma_{11} = \sigma_{22}$.

The simulation results at $\varepsilon_0^p = 0.002$ and 0.005 tended to underestimate the experimental results regardless of the model used. This discrepancy was due to the fact that yield elongation was not modeled in the simulation; thus, the stresses at yielding were smaller in the simulation than in the experiment, as also observed in Fig. 5. In contrast, the predictive accuracy at larger strains was better than that of the lower strains regardless of the model. To evaluate the predictive accuracy of anisotropic hardening quantitatively, the evolution of the shape ratio, L/L_0, was examined, where L and L_0 denote the current distance from the origin to a stress point and the distance at $\varepsilon_0^p = 0.05$, respectively, as shown in Fig. 10(a). Figure 10(b), 10(c), 10(d), and 10(e) show the evolution of the shape ratios for the stress ratios σ_{11}:σ_{22} = 4:1, 2:1, and 1:1 obtained for the experiment, the A model, the D-1 model, and the D-2 model, respectively. It should be noted that the initial trend to a strain of 0.01 is not discussed because the simulation results did not agree with the experimental results due to yield elongation, as explained earlier. In the experimental results, the shape ratios tended to decrease throughout the process regardless of the stress ratio, representing the shrinking trend of the contour of plastic work. These results were consistent with those reported for other Al alloys.[23,26)]

In the simulation, the evolution of shape ratios varied depending on the model. The shape ratios remained almost constant for the A model. Similar results have been reported in Yoshida *et al.*[23)] For the D-2 model, the shape ratios slightly decreased with the increase of plastic strain irrespective of the stress ratio. In contrast, for the D-1 model, the shape ratio slightly increased for σ_{11}:σ_{22} = 1:1 although it decreased for σ_{11}:σ_{22} = 2:1 and 4:1, which was inconsistent with the experimental results. These results suggested that, from the viewpoint of anisotropic hardening under biaxial tension, the predictive accuracies of the D models were better than the A model. Moreover, the interaction matrix parameters identified using dislocation dynamics simulations (the D-2 model), would be slightly better than in the case where all parameters were set to be the same (the D-1 model). Again, these results were consistent with those reported in the prior literature.[23)] The amounts of change in the shape ratios were much smaller for all the models than for those of the experiment; thus, the models can be further improved.

5. Discussion

5.1 Comparison between models

The results for tension and reverse loading obtained using the A model were in good agreements with those of the D models, whereas the stress–strain curve under simple shear was slightly better than that of the D models. These results suggested that at least for uniaxial loadings, the A model was applicable if a hardening law was properly selected. In

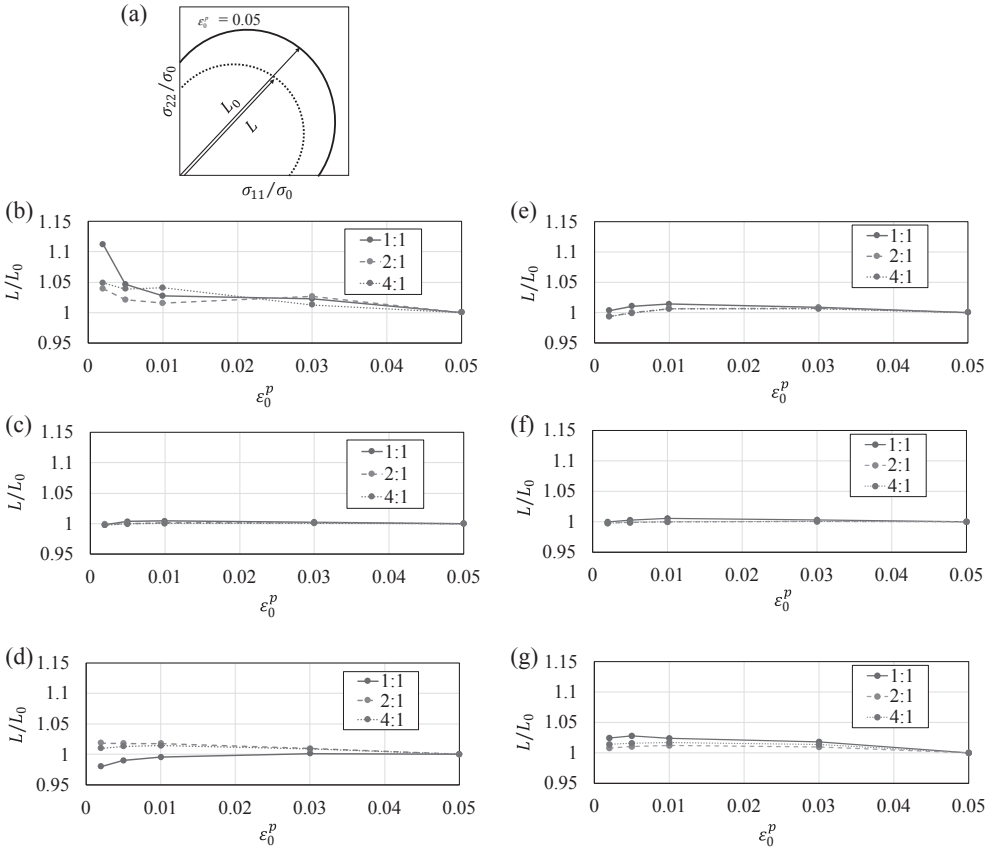

Fig. 10 Evolution of shape ratio L/L_0 as a function of ε_0^p. (a) Schematic diagrams of L and L_0, (b) experimental results, (c) A model, (d) D-1 model, (e) D-2 model, (f) E-1 model, and (g) E-2 model.

contrast, the D models represented anisotropic hardening under biaxial tension, whereas the A model was not able to reproduce it. The D-2 model was slightly better than the D-1 model in terms of anisotropic hardening in equibiaxial tension. Therefore, among the models tested in this work, the D-2 model would be more appropriate than other two models. Yoshida *et al.*[23] reached a similar conclusion from the results of biaxial tension, but in the present study it is shown for the first time that this conclusion holds not only for biaxial tension but also for various other loading conditions including uniaxial tension, reverse loading, and simple shear. The difference in the predictive accuracies between the models will be discussed more in detail in the next sections.

5.2 Effects of latent hardening and interaction matrix

When the D models were used, the difference in interaction matrix parameters hardly affected work-hardening behavior under uniaxial loadings, whereas it had a slight effect on the anisotropic work-hardening behavior under biaxial tension. As explained earlier, the parameters identified by using dislocation dynamics simulations yielded appropriate anisotropic hardening for $\sigma_{11}{:}\sigma_{22} = 1{:}1$. Very recently, Hama *et al.*[58] reported that anisotropic work-hardening under biaxial tension of a steel sheet (bcc metal) could be generated with interaction matrix parameters with anisotropic properties and could be qualitatively reproduced if different CRSSs were assigned to the {110} and {112} slip systems. This result suggested that differences in mechanical properties between the slip systems, including CRSS, work-hardening, and latent hardening/interaction, should be properly modelled to enable accurate prediction of anisotropic work-hardening under biaxial loading, consistent with the present simulation results.

It should be noted that the anisotropic hardening observed in the present material is much smaller than that observed in the steel sheet[58] in the strain range examined in this work. This difference between the fcc and bcc metals occurs presumably because multiple families of slip systems are active in bcc metals; thus, the differences in CRSS and work-hardening between the multiple families of the slip systems would play an important role in anisotropic hardening. This assumption in turn suggests that, to further improve the predictive accuracy of anisotropic work-hardening under biaxial tension in the present Al alloy sheet, the effect of factors other than latent hardening/interaction should also be considered. One of them would be the effect of yield elongation on the experiment. As discussed earlier, large discrepancies were observed in the initial stages of stress–strain curves and plastic contours between the experimental and simulation results because of yield elongation. This difference should also affect the predictive accuracy of anisotropic hardening for large strains. Therefore, it is necessary to examine predictive accuracy for other Al alloy sheets that do not exhibit either yield elongation or serrated flow. This research will be conducted as a part of future work.

5.3 Extension of accumulated-slip-based model

The difference in the predictive accuracy of anisotropic hardening under biaxial tension between the A and D models appeared presumably because the evolution of accumulated slip was almost independent of the stress path for the A model, whereas the evolution of dislocation density was dependent on the stress path for the D models.[23] This could be explained with respect to the evolution laws as follows. In the A model, because accumulated slip $\bar{\gamma}$ is not calculated separately for each slip system but is calculated by taking simply the sum of all slip systems, it is difficult to consider the effect of the difference in slip activities between the slip systems on the evolution of slip resistance of each slip system. In contrast, in the D models, the evolution of dislocation density of the α slip system is determined by the slip rate of the α slip system (eq. (6)); thus, the accumulated dislocation density can depend on the slip system. Moreover, because the accumulated dislocation density of each slip system can affect separately the hardening moduli matrix $h_{\alpha\beta}$, as described by eq. (5), the components of $h_{\alpha\beta}$ can vary depending on the dislocation density of each slip system. As a result, the evolution of slip resistance of each slip system can also depend strongly on each slip activity. This difference in the formulations could eventually affect the difference in the predictive accuracy of anisotropic hardening.

One of the practical approaches to represent anisotropic hardening by using the A model is to use the following equation for the rate of slip resistance: $\dot{\tau}_Y^{(a)} = \sum_\beta g_{\alpha\beta} h |\dot{\gamma}^{(\beta)}|$ instead of eq. (2), as in literature.[38] In fact, this equation could yield successfully anisotropic hardening under biaxial tension of hcp metals.[56,59] However, the advantages would be much less pronounced for fcc metals from the following reason. Because the material parameters of CRSSs and work hardening depend on the family of slip systems in hcp metals, h and $\dot{\gamma}^{(\beta)}$ in the abovementioned equation should differ depending on the slip systems. Therefore, in hcp metals, the difference in the evolution of slip resistance depending on the slip system would primarily result from the differences in h and $\dot{\gamma}^{(\beta)}$, although $g_{\alpha\beta}$ could also yield anisotropic hardening to some extent. In contrast, because the same material parameters were used regardless of the slip system for the present Al alloy sheet, the differences in h and $\dot{\gamma}^{(\beta)}$ would be much smaller than those of hcp metals.

On the basis of the abovementioned discussion, it is presumed that an accumulated-slip-based hardening model can be used to represent anisotropic hardening for fcc metals if the evolution of the accumulated slip is evaluated separately for each slip system. To consider this, the following extended form of the evolution law of accumulated slip is proposed: $\bar{\gamma}^\alpha = \sum_\beta \int_0^t g_{\alpha\beta} |\dot{\gamma}^\beta|$, which is used instead of $\bar{\gamma} = \sum_\alpha \int_0^t |\dot{\gamma}^\alpha|$ in eq. (4). Because $\bar{\gamma}^\alpha$ no longer represents purely accumulated slip but includes the effect of latent hardening, it is termed the effective accumulated slip in this paper. $\bar{\gamma}^\alpha$ allows considering the effect of the difference in slip activity between the slip systems on hardening; thus, the evolution of slip resistance would also depend on the slip system.

The extended model was used to simulate anisotropic hardening under biaxial tension to support the hypothesis. For simplicity, the parameters of $g_{\alpha\beta}$ for the D-1 and D-2 models were used. The extended model with the parameters of $g_{\alpha\beta}$ for the D-1 and D-2 models are referred to as the E-1 and E-2 models, respectively. The hardening parameters calibrated for the E-1 and E-2 models are shown in Table 1. The stress–strain curves under uniaxial tension using the E-1 and E-2 models are shown in Fig. 5.

When the E-2 model was used, as shown in Fig. 9(e) and Fig. 10(g), apparent anisotropic hardening appeared under biaxial tension for σ_{11}:σ_{22} = 1:1, 2:1, and 4:1, which was larger than that of the A model and comparable to that of the D models. Additionally, the shrinking trend of the contour of plastic work was represented as in the case of the D-2 model. In contrast, when the E-1 model was used, anisotropic hardening was negligible (Fig. 9(d) and Fig. 10(f)), as in the case of the A model. As we expected, the parameters of $g_{\alpha\beta}$ had clear effects on the anisotropic work-hardening behavior under biaxial tension, which is consistent with the D model and supports the hypothesis. These results indicate that the predictive accuracy of anisotropic hardening is more affected by modelling of the latent hardening and interaction matrix than by the choice of internal variables of hardening, i.e., accumulated slip or dislocation density.

The performance of the E-1 and E-2 models for simple shear are also examined, see Fig. 8. The curves of the E-1 and E-2 models were similar to that of the A model to a shear strain of approximately 0.04. However, the subsequent work hardening of the E-1 and E-2 models was much more pronounced; thus, the shear stresses were evidently overestimated. This result exhibits that the parameters of $g_{\alpha\beta}$ were not appropriate for simple shear; thus, work hardening under simple shear can be alternative reference results to determine the parameters of $g_{\alpha\beta}$.

Interestingly, the difference in the curves of the E-1 and E-2 models was more pronounced than that of the D-1 and D-2 models, exhibiting that the effects of the parameters of $g_{\alpha\beta}$ differed between the D and E models both for biaxial tension and simple shear. This further suggests that the determination of the parameters of $g_{\alpha\beta}$ also depends on the model used. It should be noted that, as an alternative approach, similar effects are also expected if the hardening parameters in eq. (4) are considered to depend on the slip system. Applications of this approach will also be studied in our future work.

6. Conclusion

In this study, crystal plasticity models that were suitable to reproduce the work-hardening behavior of an A5083-O Al alloy sheet under various loading paths, including uniaxial tension, reverse loading from compression to tension, simple shear, and biaxial tension, were studied. The conclusions obtained in this study are summarized below.

(1) The classical accumulated-slip-based hardening model with the extended Voce hardening law (A model) provided the good predictive accuracy for work-hardening behavior under uniaxial tension, reverse loading from compression to tension, and simple shear. However, it could not reproduce anisotropic hardening under biaxial tension observed in the experimental results.

(2) The dislocation-density-based hardening models (D models) used in this study reproduced the work-hardening behavior under both uniaxial loadings and biaxial tension fairly well. The results were, however, slightly more precise when the anisotropic property in the components of the interaction matrix was taken into consideration (D-2 model). From the abovementioned results, the D-2 model would be more appropriate than the other two models for the present material.

(3) A new accumulated-slip-based hardening model was proposed, in which the effect of latent hardening was considered in the calculation of accumulated slip. The new model represented anisotropic hardening under biaxial tension, which was comparable to that achieved in the D models. This result suggests that the predictive accuracy of anisotropic hardening is more affected by the modelling of the latent hardening and interaction matrix than by the choice of internal variables of hardening, i.e., accumulated slip or dislocation density.

Acknowledgements

The authors deeply acknowledge Mr. Sohei Uchida of the Osaka Research Institute of Industrial Science and Technology for his help on conducting the EBSD measurements. This study was partially supported by the Amada Foundation Grant number AF-2019004-A3 and JSPS KAKENHI Grant number 20H02480. The biaxial tensile experiments were conducted using the apparatus originally developed in Tokyo University of Agriculture and Technology (Prof. Kuwabara's laboratory), which was now transferred to Kyoto University.

REFERENCES

1) F.H. Froes, D. Eliezer and E. Aghion: JOM **50** (1998) 30–34.
2) J. Hirsch: Mater. Trans. **52** (2011) 818–824.
3) M. Asano, Y. Yamamoto and H. Takeda: UACJ Tech. Rep. **2** (2015) 107–127 (in Japanese).
4) J.F. Wang, R.H. Wagoner, W.D. Carden, D.K. Matlock and F. Barlat: Int. J. Plast. **20** (2004) 2209–2232.
5) T. Uemori, S. Sumikawa, T. Naka, N. Ma and F. Yoshida: J. JILM **65** (2015) 582–587 (in Japanese).
6) H. Wang, Y. Yan, F. Han and M. Wan: Int. J. Mech. Sci. **133** (2017) 147–166.
7) H. Takeda, A. Hibino and K. Takata: Mater. Trans. **51** (2010) 614–619.
8) F. Barlat, J.M.F. Duarte, J.J. Gracio, A.B. Lopes and E.F. Rauch: Int. J. Plast. **19** (2003) 1215–1244.
9) F. Barlat, J.C. Brem, J.W. Yoon, K. Chung, R.E. Dick, D.J. Lege, F. Pourboghrat, S.H. Choi and E. Chu: Int. J. Plast. **19** (2003) 1297–1319.
10) J.W. Yoon, F. Barlat, R.E. Dick, K. Chung and T.J. Kang: Int. J. Plast. **20** (2004) 495–522.
11) J.W. Yoon, F. Barlat, J.J. Gracio and E. Rauch: Int. J. Plast. **21** (2005) 2426–2447.
12) H. Wang, Y. Yan, M. Wan and X. Wu: Int. J. Solids Struct. **49** (2012) 3693–3710.
13) D. Yanaga, T. Kuwabara, N. Uema and M. Asano: Int. J. Solids Struct. **49** (2012) 3488–3495.
14) X. Chu, L. Leotoing, D. Guines and E. Ragneau: Int. J. Mech. Sci. **78** (2014) 27–34.
15) S. Dhara, S. Basak, S.K. Panda, S. Hazra, B. Shollock and R. Dashwood: J. Manuf. Process. **24** (2016) 270–282.
16) T. Kuwabara, T. Mori, M. Asano, T. Hakoyama and F. Barlat: Int. J. Plast. **93** (2017) 164–186.
17) H. Tian, B. Brownell, M. Baral and Y.P. Korkolis: Int. J. Mater. Form. **10** (2017) 329–343.
18) H.H. Nguyen, T.N. Nguyen and H.C. Vu: Int. J. Fract. **209** (2018) 143–162.
19) K. Zhang, B. Holmedal, O.S. Hopperstad and S. Dumoulin: Model. Simul. Mater. Sci. Eng. **22** (2014) 1–20.
20) K. Zhang, B. Homedal, O.S. Hopperstad, S. Dumoulin, J. Gawad, A. Van Bael and P. Van Houtte: Int. J. Plast. **66** (2015) 3–30.
21) A.P. Brahme, K. Inal, R.K. Mishra and S. Saimoto: Comput. Mater. Sci. **50** (2011) 2898–2908.
22) L. Hu, A.D. Rollett, M. Iadicola, T. Foecke and S. Banovic: Metall. Mater. Trans. A **43** (2012) 854–869.
23) K. Yoshida, A. Ishii and Y. Tadano: Int. J. Plast. **53** (2014) 17–39.
24) M. Luo and G. Rousselier: Int. J. Plast. **53** (2014) 66–89.
25) M. Zecevic and M. Knezevic: Int. J. Plast. **72** (2015) 200–217.
26) K. Hashimoto, A. Yamanaka, J. Kawaguchi, T. Sakurai and T. Kuwabara: J. JILM **65** (2015) 196–203 (in Japanese).
27) T. Kuwabara: Int. J. Plast. **23** (2007) 385–419.
28) T. Hama, H. Nagao, A. Kobuki, H. Fujimoto and H. Takuda: Mater. Sci. Eng. A **620** (2015) 390–398.
29) S. Bouvier, H. Haddadi, P. Levée and C. Teodosiu: J. Mater. Process. Technol. **172** (2006) 96–103.
30) J. Peirs, P. Verleysen and J. Degrieck: Exp. Mech. **52** (2012) 729–741.
31) T. Hama, T. Nishi, M. Oka, T. Matsuno, Y. Okitsu, S. Hayashi, K. Takada and H. Takuda: ISIJ Int. **61** (2021) 1971–1979.
32) S. Onaka: Philos. Mag. Lett. **90** (2010) 633–639.
33) J.S. Choi, J.W. Lee, J.-H. Kim, F. Barlat, M.G. Lee and D. Kim: Int. J. Mech. Sci. **98** (2015) 144–156.
34) ISO 16842: 2014, Metallic materials –Sheet and strip –Biaxial tensile testing method using a cruciform test piece.
35) T. Kuwabara, S. Ikeda and K. Kuroda: J. Mater. Process. Technol. **80–81** (1998) 517–523.
36) Y. Hanabusa, H. Takizawa and T. Kuwabara: J. Mater. Process. Technol. **213** (2013) 961–970.
37) T. Hama, T. Nagata, C. Teodosiu, A. Makinouchi and H. Takuda: Int. J. Mech. Sci. **50** (2008) 175–192.
38) T. Hama and H. Takuda: Int. J. Plast. **27** (2011) 1072–1092.
39) T. Hama, R. Matsudai, Y. Kuchinomachi, H. Fujimoto and H. Takuda: ISIJ Int. **55** (2015) 1067–1075.
40) J.W. Hutchinson: Proc. R. Soc. London, Ser. A **348** (1976) 101–127.
41) D. Peirce, R.J. Asaro and A. Needleman: Acta Metall. **31** (1983) 1951–1976.
42) R.J. Asaro and A. Needleman: Acta Metall. **33** (1985) 923–953.
43) J.W. Hutchinson: Proc. R. Soc. London, Ser. A **319** (1970) 247–272.
44) U.F. Kocks: Metall. Trans. **1** (1970) 1121–1143.
45) U.F. Kocks and H. Mecking: Prog. Mater. Sci. **48** (2003) 171–273.
46) C. Tomé, G.R. Canova, U.F. Kocks, N. Christodoulou and J.J. Jonas: Acta Metall. **32** (1984) 1637–1653.
47) C.N. Tomé, R.A. Lebensohn and C.T. Necker: Metall. Mater. Trans. A **33** (2002) 2635–2648.
48) J. Liu, W. Xiong, A. Behera, S. Thompson and A.C. To: Int. J. Solids Struct. **112** (2017) 35–42.
49) C. Teodosiu, J.L. Raphanel and L. Tabourot: Proc. Int. Seminar MECAMAT'91, (A.A. Balkema, Rotterdam Brookfield, 1993) pp. 153–168.
50) C. Teodosiu: *Large Plastic Deformation of Crystalline Aggregates*, (Springer-Verlag, Wien New York, 1997) pp. 21–80.
51) P. Franciosi and A. Zaoui: Acta Metall. **30** (1982) 1627–1637.
52) R. Madec, B. Devincre, L. Kubin, T. Hoc and D. Rodney: Science **301** (2003) 1879–1882.
53) B. Devincre, L. Kubin and T. Hoc: Scr. Mater. **54** (2006) 741–746.
54) L. Kubin, B. Devincre and T. Hoc: Acta Mater. **56** (2008) 6040–6049.
55) R. Madec and L. Kubin: Acta Mater. **126** (2017) 166–173.
56) T. Hama and H. Takuda: Comput. Mater. Sci. **51** (2012) 156–164.
57) G. Simmons and H. Wang: *Single Crystal Elastic Constants and Calculated Aggregate Properties: A Handbook*, Second Ed., (MIT Press, Cambridge, Massachusetts, and London, England, 1971) p. 4.
58) T. Hama, H. Fujimoto and H. Takuda: Proc. Manuf. **15** (2018) 1808–1815.
59) T. Hama, A. Kobuki and H. Takuda: Int. J. Plast. **91** (2017) 77–108.